NEW TOOLS AND METHODS FOR PRECISION SEAFLOOR MAPPING

By Chris Roman, Gabrielle Inglis, Ian Vaughn, Clara Smart, Donald Dansereau, Daniel Bongiorno, Matthew Johnson-Roberson, and Mitch Bryson

The imaging and mapping capabilities of the ROV *Hercules* have been developed over the past several years to offer multisensor data products with centimeter-scale resolution. The standard suite of mapping sensors now includes 1,375 kHz BlueView Technologies multibeam, color and black-and-white 12-bit 1,360 × 1,024 Prosilica stereo cameras, along with a 100 mW 532 nm green laser sheet and dedicated black and white camera, all of which can be run simultaneously (Figure 1). During the 2012 field season, a Raytrix R5 light field camera and an Ocean Optics STS Microspectrometer were also tested. Mapping data products were created on each cruise of the 2012 season at sites ranging from ancient shipwrecks to a vertical escarpment at Eratosthenes Seamount.

A significant result of *Nautilus* work in the Mediterranean is an array of images and maps of ancient shipwreck sites found during expeditions. Such sites have proven to be excellent test cases for the development of our mapping system. The complexity of the sites, which typically contain objects of relatively common man-made geometries, is ideal for evaluating the data collection and algorithm development. At the end of the 2012 season, we revisited many of the wreck sites previously found around the Bodrum and Datça Peninsulas in southwestern Turkey (Brennan et al., 2012). Between 2009 and 2012, many of the wrecks in this area were mapped as our surveying capabilities were being developed. The 2012 season provided an opportunity to image nearly all of the sites again with our current tools. During three days of operations, we were able to map 22 sites with some combination of stereo imaging, multibeam acoustics, and structured light

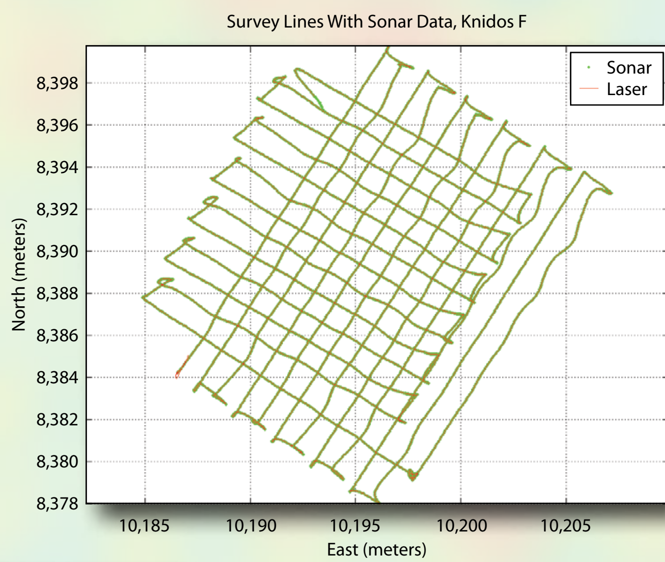

Figure 2. Vehicle trajectory for the Knidos F survey.

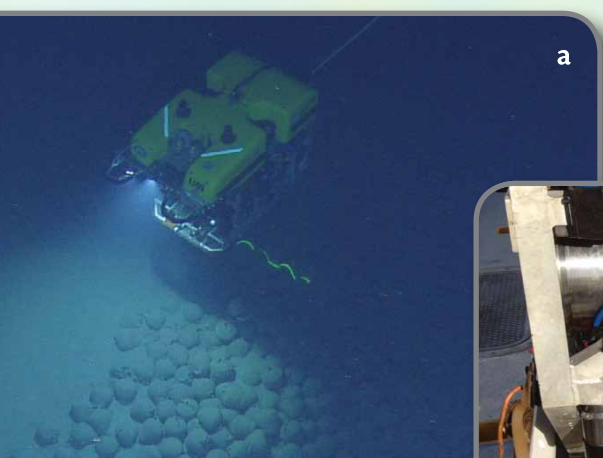

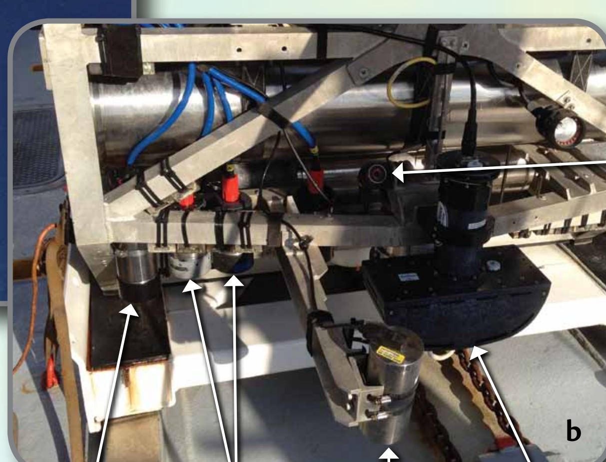

Laser Camera

Light Field Camera

Stereo Cameras

Green Laser

BlueView Sonar

Figure 1. (a) A *Hercules* laser survey. (b) The arrangement of mapping sensors on the *Hercules* remotely operated vehicle.

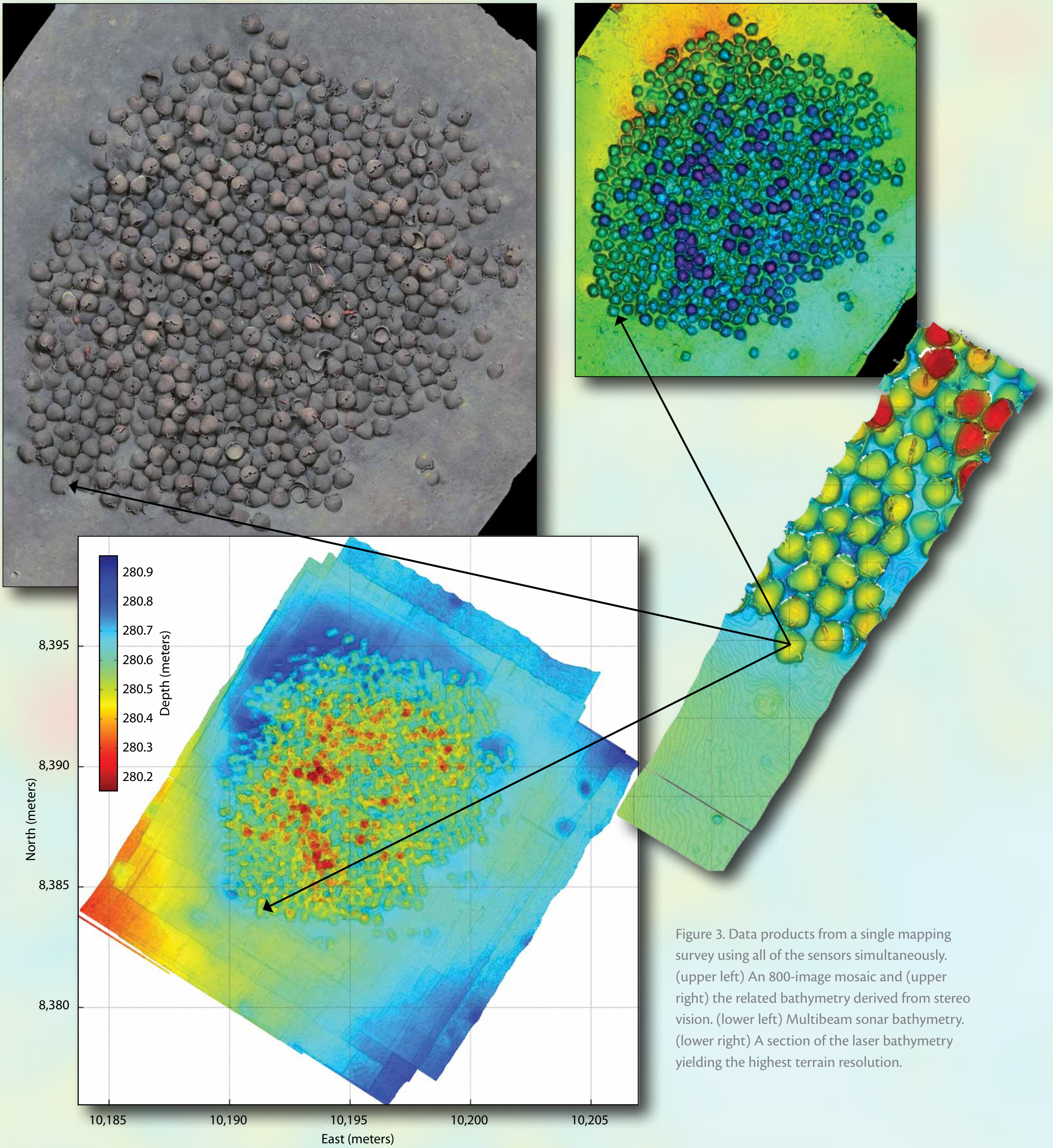

Figure 3. Data products from a single mapping survey using all of the sensors simultaneously. (upper left) An 800-image mosaic and (upper right) the related bathymetry derived from stereo vision. (lower left) Multibeam sonar bathymetry. (lower right) A section of the laser bathymetry yielding the highest terrain resolution.

laser imaging. Our current system, which can run all three technologies at once, provided a significant gain in efficiency over previous years. We mapped almost all of the sites, generally ~10 × 30 m in area, in under an hour each. The surveys were typically designed to achieve more than 200% overlapping coverage with the cameras and swath multibeam. Several sites were surveyed in a "checkerboard" pattern of overlapping and orthogonal track lines to provide multiple vantage points and reduce occlusions in the complex scenes (Figure 2). Available data products include stereo photomosaics, stereo-derived bathymetry, multibeam sonar bathymetry, and laser bathymetry (Figure 3). Navigation processing for photomosaics and bathymetric maps relies on recently developed Simultaneous

Localization And Mapping (SLAM) algorithms. These approaches filter vehicle navigation measurements from the RDI Doppler velocity log (DVL), Paroscientific depth sensor, and IXSEA Octans fiber-optic gyroscope using constraints derived from the camera images, multibeam sonar, or laser data. The result is a better-constrained navigation solution. For the stereo-vision products, we used a SLAM algorithm (Mahon et al., 2008) to estimate the position of the camera rig for each pair of stereo images. Once this action is completed, a second refinement step optimizes the positions to further reduce errors associated with reprojecting scene points visible from multiple camera locations back into their original images using a stereo bundle adjustment algorithm. This step results in a globally optimized set of camera positions, given the visual features, and reduces the negative effects of linearization in the SLAM filter. This step also refines the lens distortion calibration parameters that are applied to each image during point projections. The improvement in point consistency suggests the method is compensating for small parameter changes that occur due to the pressure forces on the camera housing while operating in deep water.

This final result is used to generate the full-vision-based structural model used for reconstruction. We employ a previously developed scene reconstruction technique (Johnson-Roberson et al., 2010) with a modification to operate in full three dimensions. This step is needed to preserve the visual quality of the model in the highly structured wreck scenes. Through the use of state-of-the-art model parameterization and texture antialiasing, distortions in the final result can be minimized while maintaining the resolution of the original source imagery in the complete mosaic (Lévy et al., 2002; Sheffer et al., 2005). The mosaic can be displayed as a downward projection, or draped on the scene structure as a textured three-dimensional model.

For the bathymetry maps, we continue to use a SLAM algorithm that creates short sequences of multibeam pings or laser line profiles to match the terrain and refine the navigation estimates (Inglis et al., 2012). The same concept applies for both multibeam bathymetry, which provides the most sensor coverage, and structured light laser data, which provide the highest resolution. The ability to collect mapping data simultaneously from several sensors supplies a direct way to compare results and makes the fusion of visual and acoustic data possible.

We completed surveys similar to those conducted on shipwreck sites (Figure 3) at many other complex sites in 2012 (e.g., see discussion of the seamounts of the Anaximander Mountains on page 30 and Eratosthenes Seamount on page 36). While working at Eratosthenes Seamount, we again found a significant number of gouges on the flat and mostly featureless seafloor. They are thought to be caused by foraging of Cuvier's beaked whales. The markings were present along several of the visual transects and also observed in the side-scan sonar. The side-scan data are currently being reviewed to estimate the spatial density of the marks. To better characterize the patterning of the marks, we compiled three separate high-resolution photomosaics in areas with both fresh and aged marks. The mosaics indicate a consistent pattern for gouges of similar apparent age. Several sequences of at least three to six marks have been observed, all with the same approximate spacing (Figure 4). This pattern seems to indicate a single animal making repeat gouges in the seafloor on a single dive. Across all three sites, the spacing and curvilinear arrangement were observed, and the mosaics provided a new look at these features. We took several push cores in these survey areas to evaluate the sediment content. We are looking at the cores, side-scan data, and this new observation of the patterning to evaluate whether the gouges are in fact related to a feeding behavior.

In an effort to investigate new imaging technologies, we packaged a light field camera and used it to collect evaluation images. Also known as plenoptic cameras, light field cameras offer a range of impressive post-capture capabilities, including depth estimation and filtering (Dansereau and Bruton, 2004), noise reduction (Dansereau et al., 2013), video stabilization (Smith et al., 2010), and isolation of distractors (such as fish, drifting organisms, swaying vegetation, and dynamic lighting; Dansereau and Williams, 2011). The cameras' optics also simultaneously offer wide aperture and wide depth of field imaging compared with conventional cameras (Ng et al., 2005; Bishop and Favaro, 2012). The goals of these first field trials were to establish the viability of using light field cameras in underwater applications and to confirm some of the theoretical advantages they present. The camera we employed was a commercially available Raytrix f/2.4 4-megapixel monochrome light field camera. We tested it at the shipwreck sites in the Bodrum area and compared the photos directly with those taken using conventional cameras.

Conditions were generally favorable for imaging, with mostly clear water and the occasional appearance of stirred up sediment that reduces the image quality due to back-scatter in proportion to light intensity. For this reason, we were particularly interested in the light field camera's improved light gathering ability. To test the camera, we mounted it alongside the conventional cameras, but operated it with less than half (roughly 0.4 times) the illumination. The light field camera performs well despite the significant reduction in illumination power (Figure 5). The camera's achievable depth of field was also confirmed by imaging over a range of altitudes. One capture provides the ability to computationally manipulate the image focal depth during post processing and to direct attention to any distance between the camera and the seafloor (Figure 6). These initial deployments yielded experimental support for the enhanced light gathering and depth filtering capabilities of light field cameras. Looking ahead, we expect these attributes to present a significant advantage in reducing illumination power budgets, increasing imaging ranges, or allowing better images in turbid conditions with water column distractors. During the off season, additional experiments

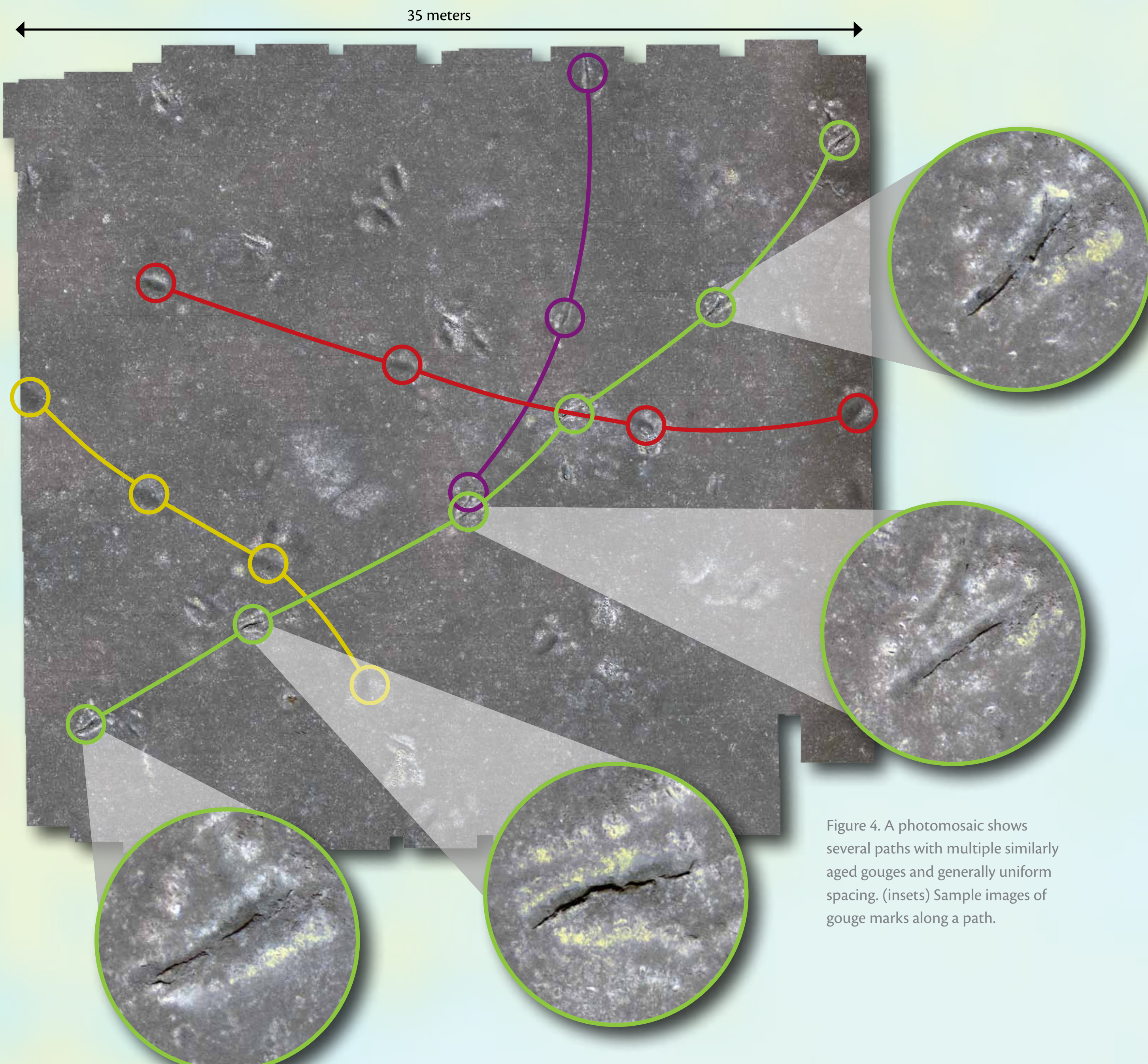

Figure 4. A photomosaic shows several paths with multiple similarly aged gouges and generally uniform spacing. (insets) Sample images of gouge marks along a path.

will be performed in a test tank to better understand the camera's in-water performance.

During the 2012 field season, we also incorporated a downward-facing spectrometer into the camera system. Spectrometers are point measuring hyperspectral optical devices. The STS Microspectrometer tested was capable of detecting 1,024 bands of light within the near ultraviolet/visible/near infrared spectrum in the range of 330–830 nm. Measurements with the spectrometer were taken simultaneously with the downward-facing stereo cameras during several surveys. We were able to collect measurements at three sites: a bacterial mat site near the Athina Mud Volcano, a Byzantine shipwreck, and the site of the gouge marks (Figure 4). The high spectral resolution available with the spectrometer allows for greater discrimination of bottom type, as different materials often exhibit subtle differences in their spectral reflectance. Because the spectrometer is only a point-measuring device, we obtain one large pixel

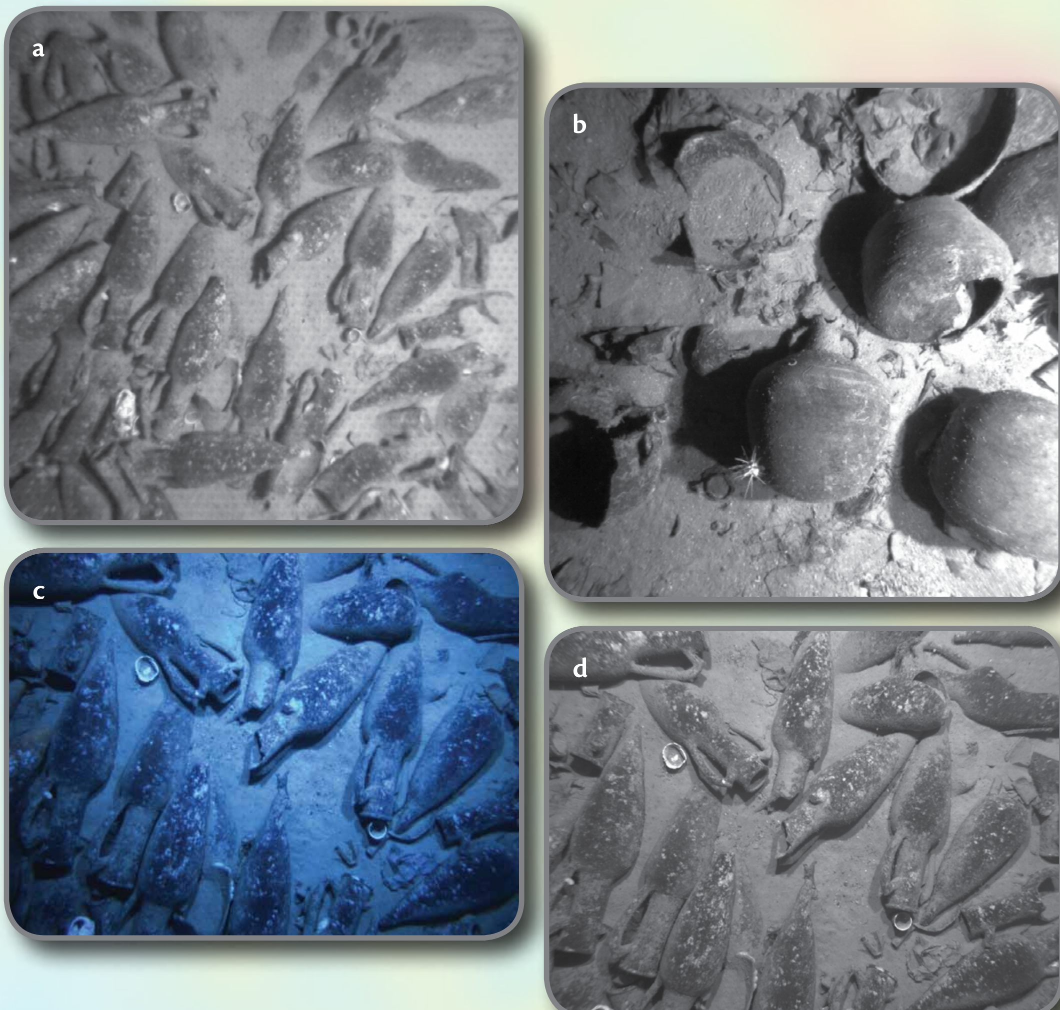

Figure 5. Test images of amphorae show the potential of light field cameras to facilitate underwater imaging. Light field imagery (a,b) required roughly 0.4 times the illumination needed for the conventional color (c) and monochrome (d) imagery.

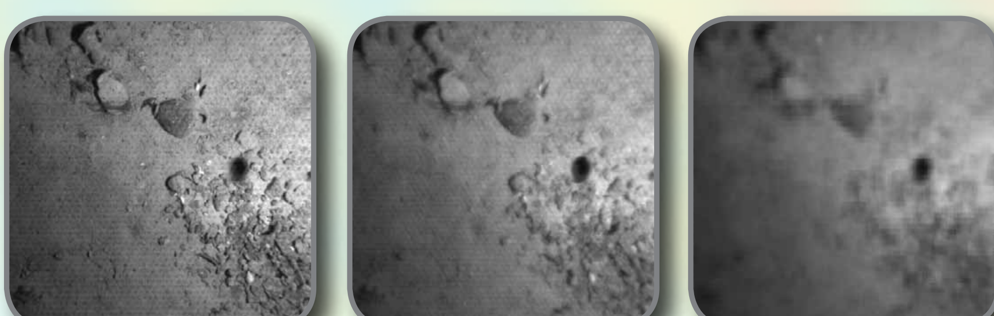

Figure 6. Images created from a single light field capture. (left) Image created at the calibrated focal depth with the seafloor in focus. (middle) Image focused at the black particle in the mid water. Note the seafloor is out of focus. (right) Image focused in the very near field, leaving the bottom and particle out of focus.

for each image location such that multiple materials can be “mixed” within the one pixel footprint. In the remote-sensing realm, there are techniques to spectrally unmix the material constituents of that pixel. Using this information, we are able to determine the fractional abundances of each material/end member within the pixel. Our initial results from the Athina bacterial mat data set show we are able to unmix the spectral data to resolve the abundance of the materials within the scene. We used the N-FINDR algorithm (Winter, 1999) to resolve the most pure end members in the data set. The extracted end members are not necessarily pure in their material makeup but rather the most spectrally distinctive from the other measured spectra. The spectra of the end members were found, along with the corresponding RGB imagery (Figure 7). We are further processing these data sets, including using the stereo RGB image data to assist in the spectral unmixing. These initial results show we can gather high spectral measurements alongside the high spatial resolution imagery from the RGB cameras.

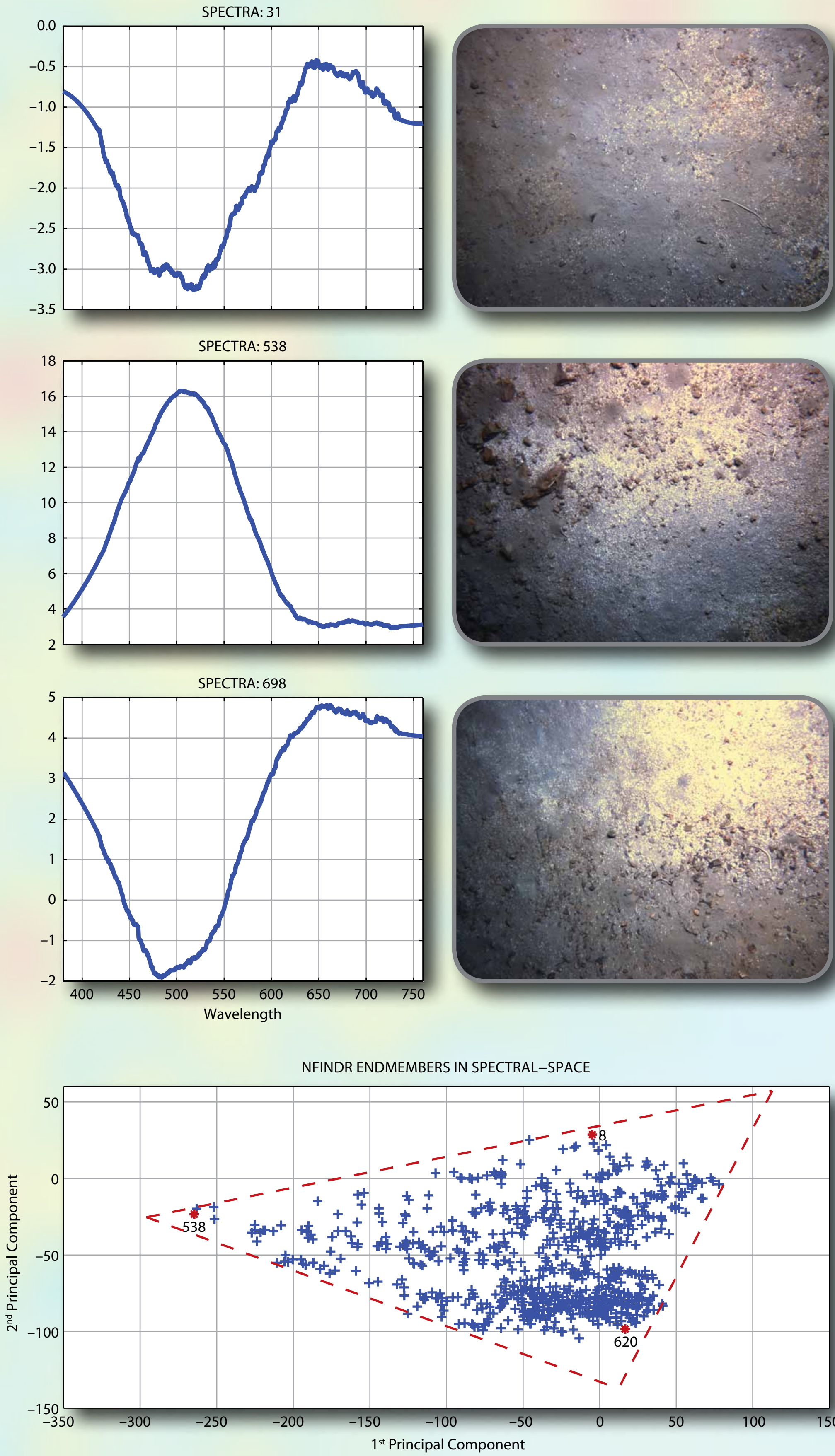

Figure 7. Example images and the accompanying spectra that are end members of the set of collected images within a survey.